Applied Physics Letters

RESEARCH ARTICLE | AUGUST 20 2024

Effective InAsP dislocation filtering layers for InP heteroepitaxy on CMOS-standard (001) silicon

Shangfeng Liu; Bogdan-Petrin Ratiu ; Hui Jia ; Zhao Yan ; Ka Ming Wong ; Mickael Martin ; Mingchu Tang; Thierry Baron ; Huiyun Liu ; Qiang Li

Appl. Phys. Lett. 125, 082102 (2024)
https://doi.org/10.1063/5.0219507

20 August 2024 16:27:56

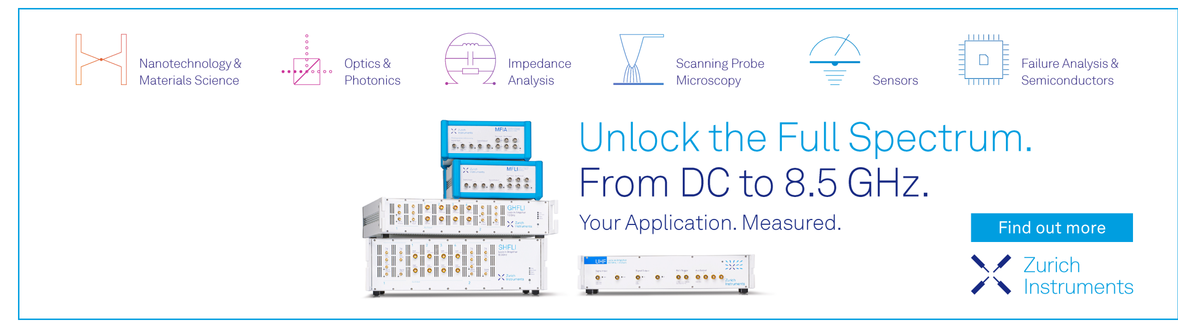

Effective InAsP dislocation filtering layers for InP heteroepitaxy on CMOS-standard (001) silicon

Cite as: Appl. Phys. Lett. **125**, 082102 (2024); doi: 10.1063/5.0219507
Submitted: 17 May 2024 · Accepted: 8 August 2024 ·
Published Online: 20 August 2024

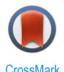

Shangfeng Liu,[1] Bogdan-Petrin Ratiu,[1] Hui Jia,[2] Zhao Yan,[1] Ka Ming Wong,[1] Mickael Martin,[3] Mingchu Tang,[2] Thierry Baron,[3] Huiyun Liu,[2] and Qiang Li[1,a)]

AFFILIATIONS

[1]School of Physics and Astronomy, Cardiff University, Cardiff, United Kingdom
[2]Department of Electronic and Electrical Engineering, University College London, London, United Kingdom
[3]University Grenoble Alpes, CNRS, CEA/LETI-Minatec, Grenoble INP, LTM, Grenoble F-38054, France

[a)]Author to whom correspondence should be addressed: LiQ44@cardiff.ac.uk

ABSTRACT

In this work, we report InAsP-based dislocation filter layers (DFLs) for InP heteroepitaxy on CMOS-standard (001) Si substrates, demonstrating a threading dislocation density of $3.7 \times 10^7\ \text{cm}^{-2}$. The strain introduced by InAsP induces dislocation bending at the InAsP/InP interface, thereby facilitating the reaction and annihilation of dislocations during their lateral glide. Concurrently, the InP spacer exhibits tensile strain, leading to the formation of stacking faults (SFs). With a comprehensive analysis utilizing x-ray diffraction, electron channeling contrast imaging, and transmission electron microscopy, the effects of DFL-induced strain on dislocations and SFs are investigated. Fine-tuning the strain conditions allowed low-dislocation-density while SF-suppressed, anti-phase boundary free InP on Si. This work, therefore, provides a useful buffer engineering scheme for monolithic integration of InP-based electronic and photonic devices onto the industry-standard silicon platform.

© 2024 Author(s). All article content, except where otherwise noted, is licensed under a Creative Commons Attribution (CC BY) license (https://creativecommons.org/licenses/by/4.0/). https://doi.org/10.1063/5.0219507

20 August 2024 16:27:56

In the last decade, the integration of III–V semiconductors on Si substrates has garnered growing attention, fueled by the need for high-performance photonic integrated circuits and advancements in communications and sensing technologies.[1–4] The demonstration of high-efficiency, long-lifetime InAs/GaAs quantum-dot O-band lasers on the GaAs-on-Si platforms shows great potential of epitaxial integration for mass production of photonic integrated devices and circuits at reduced costs.[5,6] These have motivated the further exploration of the dislocation tolerance prospect of integrating InP-based lasers, including quantum dot/well lasers,[7–10] inter-band cascade lasers,[11] and quantum cascade lasers,[12,13] on various silicon platforms by direct epitaxy. These laser are critical components for a range of important applications such as inter/intra-chip optical interconnects, long-haul fiber communication, spectroscopic sensing, medical diagnostics, etc.

Compared to GaAs heteroepitaxy on Si, direct epitaxy of InP on Si faces twice larger lattice mismatch (∼8%), which leads to a higher density of threading dislocations (TDs). Due to the bonds in InP exhibiting stronger ionicity, growing InP on Si is more susceptible to the formation of stacking faults (SFs).[14] These defects act as typical nonradiative recombination centers and consequently degrade device efficiency and increase the lasing threshold. Moreover, anti-phase boundaries (APBs), a common issue when growing polar materials (III–V) on non-polar (Si) substrates, further deteriorate the performance and reliability of the devices. To mitigate these crystalline imperfections, various techniques have been explored, including post-growth thermal cycle annealing,[15] insertion of strained superlattice/quantum-dot layers,[16,17] graded buffer,[18] and epitaxial lateral overgrowth.[19,20] Specifically, employing strained dislocation filter layers (DFLs) has been regarded as a promising approach without relying on complex substrate patterning processes. This method is capable of facilitating dislocation glide through the generation of misfit dislocations, thereby driving dislocation line with opposite Burgers vectors to annihilate.[21,22] To date, most threading dislocation density (TDD) values reported from epitaxial InP thin films on planar Si have been limited to greater than $10^8\ \text{cm}^{-2}$.[7,8,12,23] As for DFL structure, all previous research employed common-anion ternary alloys[23–26] (such as InGaP, InGaAs, and InAlAs) to induce appropriate strain, while common-cation alloys have not been studied as DFLs.

© Author(s) 2024

In this work, we achieved InP heteroepitaxy on CMOS-standard (001) Si with a low TDD $3.7 \times 10^7\,cm^{-2}$ by introducing a common-cation InAsP-based dislocation filter on an APB-free buffer template. It is found that the compressive strained InAsP layer effectively blocks TDs; however, the resultant tensile strain in the following InP growth promotes the formation of SFs. Through managing the strain state of the DFLs, we were able to reduce the density of the SFs while preserving the excellent dislocation filtering efficiency. This strategy offers a practical pathway for the integration of III–V optoelectronic devices on Si.

The material growth starts from an APB-free 170 nm InP/400 nm GaAs/Si template, which was originally grown on a 300 mm microelectronic standard nominal Si(001) by MOCVD. Details of this template preparation can be found in previous publications.[27] This 300 mm InP template was fabricated into 2-in. wafers by laser cutting for further InP epitaxy with DFLs using an AIXTRON close-coupled showerhead MOCVD reactor. Before transferred into the MOCVD reactor, the template was treated by aqueous 2.5% HF solution for 120 s to remove surface oxides and blown dry with nitrogen. The InAsP and InP layers were grown at a wafer temperature of 590 °C, using hydrogen (H_2) as carrier gas, trimethylindium (TMIn) as the group III, and tertiarybutylarsine (TBAs) and trinbutylphosphine (TBP) as the group V precursors.

The schematic presentation of the epitaxial InP/InAsP filter layer on the InP/Si substrate is depicted in Fig. 1(a). In this series, following 500 nm InP regrowth, 200 nm InAsP layers with As compositions of 10% and 24% were employed. Additionally, a reference sample with only an InP layer of 1 μm, without DFLs, was grown for comparison. The composition of InAsP was calibrated based on x-ray diffraction (XRD) with results shown in Fig. 2. Then, defect density for these samples was characterized by electron channeling contrast imaging (ECCI) scans, with the statistical results plotted in Fig. 1(b) to show the defect variation with As composition in DFL. In the ECCI channeling condition, both SFs and TDs cause changes in the intensity of backscattering electrons, resulting in noticeable contrast variations in the ECCI images. Specifically, SFs appear as line segments, while TDs appear as bright or dark spots, as typically shown in Fig. 3. This allows us to accurately identify and count these defects. To demonstrate the effect of growing thicker InP buffers and InAsP DFLs, ECCI was also performed on the starting InP on Si template, which gives a high TDD of $\sim 1.7 \times 10^9\,cm^{-2}$ [shown in Fig. 3(a)]. The reference sample without InAsP DFL shows a TDD of $8.9 \times 10^8\,cm^{-2}$, marginally lower than that of the initial InP/Si template. After inserting the InAsP layer with As composition of 10% and 24%, the TDD decreases to 6.1×10^8 and $1.9 \times 10^8\,cm^{-2}$, corresponding to 31% and 79% reduction of TDD, respectively. From the ECCI images, in addition to dislocation outcrop points, SFs manifesting as intercrossing line patterns with bright contrast also appear. Such kinds of SFs were visible in the atomic force microscopy images as well (not shown here). In this work, the SF density is defined as the ratio of the total length of all SFs to the scanning area of ECCI. By statistically analyzing the length of SFs per unit area in ECCI, we find that as the As component increases, the density of the SFs continuously rises.

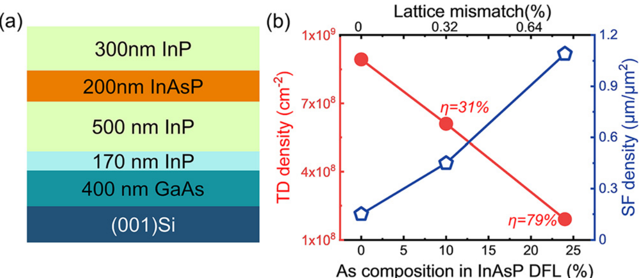

FIG. 1. (a) Schematic illustration of the dislocation filter layer structure grown on InP/GaAs/Si template, inserted with the 200 nm InAsP layer. (b) Extracted dislocation density and stacking faults density from the ECCI images as a function of the As composition in the InAsP layer.

To further explore the influence mechanism of the InAsP DFL on dislocations and SFs, samples with 1, 2, and 3 layers of DFL on InP-on-Si templates were subsequently grown, by directly adding more stacks of 200 nm $InAs_{0.24}P_{0.76}$/300 nm InP DFLs. Upon characterizing these samples with ECCI, the changes in dislocation density and SF density with the number of DFL are shown in Fig. 2(a). The insertion of more DFL layers progressively reduces the TDD. The initial layer induces the most pronounced effect in diminishing the density. Following the integration of the second layer, the TDD diminishes to $7.3 \times 10^7\,cm^{-2}$, yet the reduction in TDD approaches a plateau upon the addition of the third layer. However, the insertion of dislocation filter layers markedly leads to an increase in SF density, and all three samples exhibit similar SF densities on the order of $\sim 1\,\mu m/\mu m^2$, indicating that further addition of InAsP/InP layers does not effectively mitigate the SFs.

An XRD omega-2theta scan of the (004)-plane diffraction was performed for these samples to analyze the strain state of InP/InAsP layers. Figure 2(b) shows the omega-2theta scan of the sample with 2 InAsP DFLs, with the peak position angle of Si (004) used for alignment. According to Bragg's law, the positions of crystal plane diffraction peaks can shift due to changes in lattice constants caused by strain. By comparing the InAsP peak position with the value (31.40°) of strain-free $InAs_{0.24}P_{0.76}$, the InAsP DFLs exhibit in-plane compressive strain. Notably, two diffraction peaks for InP were observed, one of which is located at unstrained position, attributed from the underlying InP layer directly on top of the GaAs (see Fig. S1 in the supplementary material for more information). The other peak at a higher diffraction angle was correlated with the InP spacer layer grown after InAsP layers, indicating in-plane tensile strain. The evolution of XRD peak positions for InAsP and strained InP is plotted in Fig. 2(c). A notable trend is observed: InP shows a continuous increase in tensile strain as the number of DFLs increases; on the other hand, InAsP consistently exhibits an increase in compressive strain. This trend implies that with the increase in the DFL numbers, the in-plane lattice constants of the upper-layer strained InAsP/InP gradually become closer, suggesting that they progressively exhibit a lower relaxation to release strain energy.

To quantitatively calculate the strain induced by DFLs and compare the relaxation states of the InAsP and the InP layers, XRD reciprocal space mapping of (115) plane for the InP sample with two layers of DFL was also performed, as shown in Fig. 2(d). Corresponding to the two peaks in omega-2theta scan, InP shows obvious diffraction pattern split in reciprocal space, which is highlighted in the zoomed-in image [Fig. 2(e)]. A line representing full relaxation (red dashed line) is drawn here to help observe the relaxation state of the layers, clearly showing that InAsP has not achieved full relaxation. According to the

20 August 2024 16:27:56

© Author(s) 2024

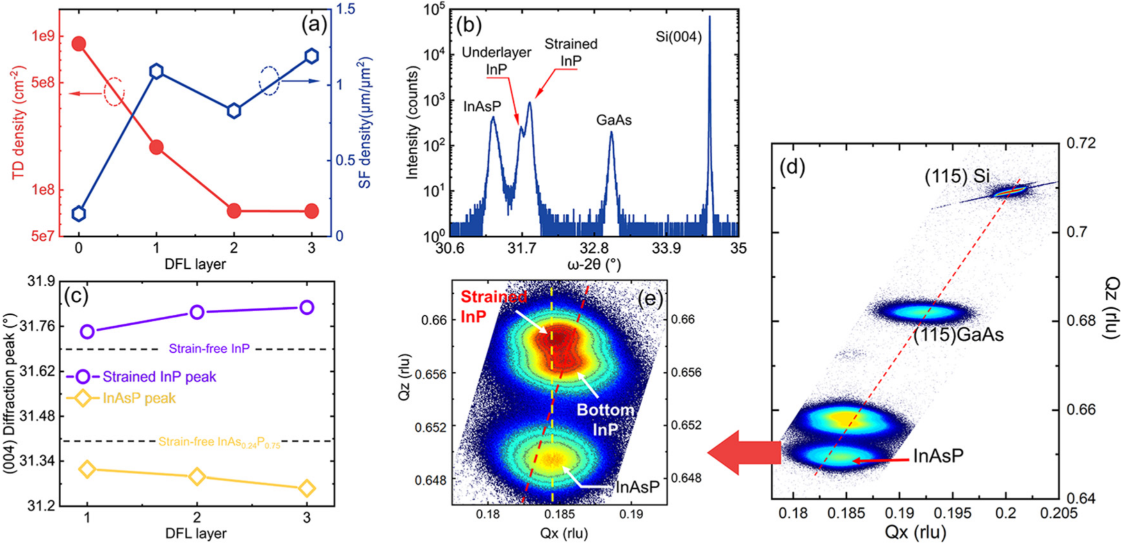

FIG. 2. (a) Extracted dislocation density and stacking fault density from the ECCI images as a function of the InAsP layer number. (b) (004) plane omega-2theta scan curve of the InP template with 2 × 200 nm DFLs. (c) Extracted (004) plane XRD peak position of tensile-strained InP and InAsP as a function of the InAsP layer number. The dashed lines indicate the positions of the (004) diffraction peaks for unstrained InP and InAsP, to assist observing the evolution of strain. (d) XRD reciprocal space mapping of (115) plane for the sample with 2 × 200 nm InAsP DFLs (the red dashed line represents the fully relaxation line). (e) A zoom-in image of the InP and InAsP pattern, in which the yellow dashed line represents the fully strained line based on InAsP.

x-ray diffraction theory, Q_x of the diffraction spot is in reverse proportion of the in-plane lattice constant a; hence, the in-plane tensile strain $\varepsilon_{//}[\varepsilon_{//} = (a_{\mathrm{InP_strained}} - a_{\mathrm{InP_strain}\,free})/a_{\mathrm{InP_strain}\,free}]$ of spacer InP is calculated to be 0.37%. Meanwhile, the relaxation of InAsP layer is calculated to be ~70% (relative to the underlying InP strain-free layer), indicating it is still partially relaxed under a 200 nm thickness. As evidenced by the strained-InP diffraction pattern's deviation from InAsP's fully strained line (yellow dashed line), the InP spacer above the InAsP undergoes a partial relaxation toward strain-free InP.

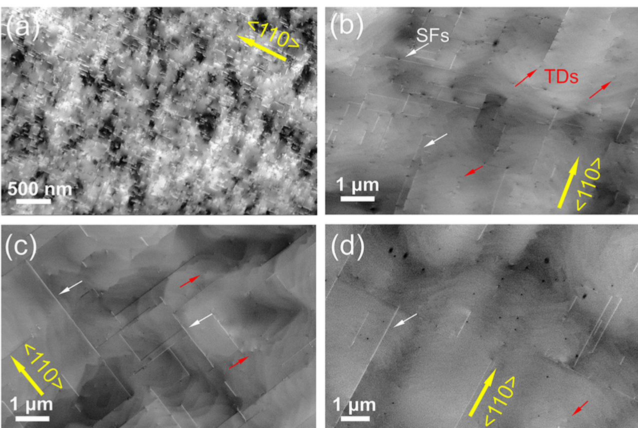

FIG. 3. The electron channeling contrast imaging of (a) the initial InP/GaAs/Si substrate without InP/InAsP epitaxy, the InP sample with (b) 1 × 200 nm InAsP layer, (c) 2 × 200 nm InAsP layer, and (d) 3 × 100 nm InAsP layer. Some example SFs are marked by white arrows, and example TDs are marked by red arrows.

To directly demonstrate the generation and propagation of the TDs and SFs in detail, cross-sectional transmission electron microscopy (TEM) images of the sample with 3 InAsP layers were characterized, as shown in Fig. 4. From an overview of the whole structure [Fig. 4(a)], plenty of TDs are generated at the interfaces of GaAs/Si and InP/GaAs, attributed to the substantial mismatch, with TDD estimated to be on the order of 10^{10} and $10^{9}\,\mathrm{cm}^{-2}$, respectively. Notably, the initial DFL layer proves to be remarkably efficient in obstructing the majority of penetrating dislocations, with few dislocation lines being observed at the top InP layer. A reduction in the effectiveness of dislocation filtering is shown in the upper layers of DFLs, as the same trend shown in Fig. 2(a). The efficiency drop in upper layers of InAsP DFL can be explained as: First, the reduced density of threading dislocations at higher DFL layers, leads to an increased average distance between the misfit dislocation network and threading dislocations, thereby reducing the possibility of meeting in a capture radius and annihilation between dislocation lines with opposite Burgers vector. As labeled with blue arrows in the TEM image Fig. 4(b), which was intentionally tilted to reveal the interfaces in projection, misfit dislocations have a longer travel distance at upper InAsP/InP interfaces (see Fig. S2 in the supplementary material for more information), suggesting fewer annihilation process happening at this stage. Second, as shown in the XRD results, the tensile strain in the InP spacer gradually increases, which leads to a reduced initial releasable compressive strain energy in the subsequently grown InAsP layers. Consequently, this indirectly results in a decreased capability to drive the TD bending at the InAsP/InP interface.

As indicated by Fig. 2(a), the SF density increases with the introduction of DFLs. This observation is further substantiated by tilted TEM observations, as shown in Figs. 4(b) and 4(c). Since SFs are planar defects, they appear as stripe-like features, allowing us to

20 August 2024 16:27:56

© Author(s) 2024

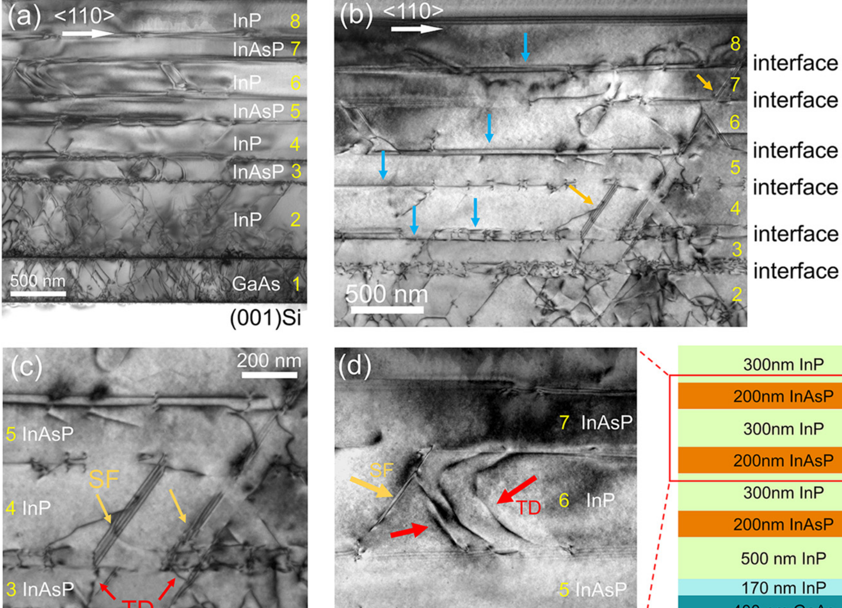

FIG. 4. (a) Cross-sectional TEM overview of the sample with 3 × 200 nm InAsP layers with on-axis. (b) and (c) Zoomed-in TEM images intentionally tilted to highlight the interfaces in projection. The SFs generation from the InP/InAsP interfaces is marked by yellow arrows, and misfit dislocations are marked by blue arrows. (d) Zoomed-in observation of the stacking faults blocking the movement of the TDs. The yellow arrow marked the SFs, and the TDs are marked with red arrows.

distinguish them from TDs, which are line-like features in tilted images. Notably, long-segment SFs are rarely observed in the underlying InP layer before the introduction of the DFL. Compared to TDs that tend to be annihilated at the growth start of InAsP, SFs appear to be more likely to emerge at the starting interfaces of the InP spacers, as labeled by yellow arrows in Fig. 4(c). It was reported when mixed-type dislocation lines glided through tensile region, they can be separated into two partial dislocations connected by an SF.[28] In our case, tensile-strained-InP plays a role to unfold mixed-type dislocation lines into SFs. The two ends of the SFs can be seen to exhibit dislocation outcrops in ECCI images. As indicated by red arrows in Fig. 4(d), we observe the dislocation blocking effect by SFs. When SFs (indicated by yellow arrows) cross the line direction of dislocations, movement of the three pileup dislocations is blocked. Dislocation loops form here and are confined within the InP spacer. They, therefore, did not increase TDD at the top surface.

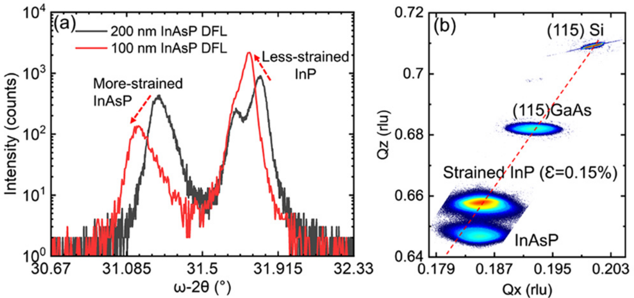

FIG. 5. (a) Comparison of XRD (004) plane omega-2theta scan curves of the InP with 3 × 200 nm DFLs and 3 × 100 nm DFLs. (b) XRD reciprocal space mapping of (115) plane for the sample with 3 × 100 nm InAsP DFLs. The red dashed line represents the fully relaxation line.

To reduce the tensile strain in InP and reduce the density of SFs, we grew samples with three layers of InAsP DFLs with reduced InAsP thicknesses of 100 nm. After characterizing with ECCI, as shown in Fig. 3(d), the TDD was observed to be further reduced to $3.7 \times 10^7\ \mathrm{cm}^{-2}$ based on a scanning area of 306 $\mu\mathrm{m}^2$, which represents one of the lowest recorded TDD values of planar InP growth on Si. Furthermore, the density of SFs was more than halved, decreasing to 0.4 $\mu\mathrm{m}/\mu\mathrm{m}^2$. In the omega-2theta scan results [Fig. 5(a)], the peak position of InP moves toward the unstrained direction, despite an asymmetrical shoulder indicating some residual strain still exists. The reduction in tensile strain in InP is believed to be the reason for the decreased density of SFs. The reduction in thickness of InAsP causes its intensity to decrease and moving toward the direction of more compressive strain. According to the results from XRD reciprocal space mapping, as shown in Fig. 5(b), the InP pattern has shrunk to a single one with a decreased strain value of 0.15%. These results corroborate the aforementioned strain analysis and highlight the importance of the co-managing the strain levels in the InAsP/InP DFLs for effectively reducing TDs and suppressing SFs.

In summary, we have studied a common-cation InAsP-based interlayer, which shows high dislocation filtering efficiency for InP heteroepitaxy on CMOS-standard (001) Si. Furthermore, we explored the influence of the InAsP DFLs on generating tensile strain in the ensuing InP layers, which, in turn, facilitates the formation of SFs. Through reduction of the strained layer thicknesses in the DFL, we achieved a reduction in both TDs and SFs, paving a practical path toward integrating APB-free, low-defect-density InP on Si for the future of III–V optoelectronic devices on silicon platforms.

See the supplementary material for more information about the strain of the reference InP sample and some zoom-in TEM images to show misfit dislocations.

20 August 2024 16:27:56

© Author(s) 2024

This work was supported in part by the Engineering and Physical Sciences Research Council (Grant No. EP/V029681/1) and the UKRI Strength in Places Fund (Grant No. 107134). This work was partly supported by the French Renatech Network. Valuable discussions with Professor R. Beanland are also acknowledged.

AUTHOR DECLARATIONS

Conflict of Interest

The authors have no conflicts to disclose.

Author Contributions

Shangfeng Liu: Conceptualization (lead); Data curation (lead); Formal analysis (lead); Investigation (lead); Methodology (lead); Project administration (lead); Visualization (lead); Writing – original draft (lead); Writing – review & editing (lead). **Bogdan-Petrin Ratiu:** Conceptualization (equal); Formal analysis (equal); Investigation (equal); Methodology (equal); Writing – review & editing (equal). **Hui Jia:** Data curation (equal); Formal analysis (equal); Methodology (equal). **Zhao Yan:** Investigation (equal); Writing – review & editing (equal). **Ka Ming Wong:** Data curation (equal); Formal analysis (equal); Investigation (equal). **Mickael Martin:** Data curation (equal); Funding acquisition (equal); Methodology (equal). **Mingchu Tang:** Data curation (equal); Formal analysis (equal); Methodology (equal). **Thierry Baron:** Data curation (equal); Funding acquisition (equal); Methodology (equal). **Huiyun Liu:** Data curation (equal); Formal analysis (equal); Methodology (equal). **Qiang Li:** Conceptualization (lead); Formal analysis (lead); Funding acquisition (lead); Investigation (lead); Methodology (lead); Project administration (lead); Supervision (lead); Writing – review & editing (lead).

DATA AVAILABILITY

Data supporting the findings of this study are available in The Cardiff University Research Portal at https://10.17035/cardiff.26561503.

REFERENCES

[1] J. Yang, M. Tang, S. Chen, and H. Liu, Light 12(1), 16 (2023).
[2] N. Margalit, C. Xiang, S. M. Bowers, A. Bjorlin, R. Blum, and J. E. Bowers, Appl. Phys. Lett. 118(22), 220501 (2021).
[3] S. Mauthe, Y. Baumgartner, M. Sousa, Q. Ding, M. D. Rossell, A. Schenk, L. Czornomaz, and K. E. Moselund, Nat. Commun. 11(1), 4565 (2020).
[4] Z. Yan and Q. Li, J. Phys. D 57(21), 213001 (2024).
[5] S. Chen, W. Li, J. Wu, Q. Jiang, M. Tang, S. Shutts, S. N. Elliott, A. Sobiesierski, A. J. Seeds, I. Ross, P. M. Smowton, and H. Liu, Nat. Photonics 10(5), 307 (2016).
[6] C. Shang, E. Hughes, Y. Wan, M. Dumont, R. Koscica, J. Selvidge, R. Herrick, A. C. Gossard, K. Mukherjee, and J. E. Bowers, Optica 8(5), 749 (2021).
[7] S. Zhu, B. Shi, Q. Li, and K. M. Lau, Appl. Phys. Lett. 113(22), 221103 (2018).
[8] B. Shi, H. Zhao, L. Wang, B. Song, S. T. Suran Brunelli, and J. Klamkin, Optica 6(12), 1507 (2019).
[9] B. Dong, J. Duan, C. Shang, H. Huang, A. B. Sawadogo, D. Jung, Y. Wan, J. E. Bowers, and F. Grillot, Appl. Phys. Lett. 115(9), 091101 (2019).
[10] K. Sears, H. H. Tan, M. Buda, J. Wong-Leung, and C. Jagadish, in Presented at the 2006 International Conference on Nanoscience and Nanotechnology (2006).
[11] K. Ryczko, J. Andrzejewski, and G. Sek, Materials 15(1), 60 (2021).
[12] S. Xu, S. Zhang, J. Kirch, H. Gao, Y. Wang, M. Lee, S. Tatavarti, D. Botez, and L. Mawst, Appl. Phys. Lett. 123(3), 031110 (2023).
[13] E. Cristobal, M. Fetters, A. W. K. Liu, J. M. Fastenau, A. Azim, L. Milbocker, and A. Lyakh, Appl. Phys. Lett. 122(14), 141108 (2023).
[14] H. Gottschalk, G. Patzer, and H. Alexander, Phys. Status Solidi A 45(1), 207 (1978).
[15] Y. Ababou, P. Desjardins, A. Chennouf, R. Leonelli, D. Hetherington, A. Yelon, G. L'Espérance, and R. A. Masut, J. Appl. Phys. 80(9), 4997 (1996).
[16] K. Samonji, H. Yonezu, Y. Takagi, K. Iwaki, N. Ohshima, J. K. Shin, and K. Pak, Appl. Phys. Lett. 69(1), 100 (1996).
[17] B. Shi, Q. Li, and K. M. Lau, J. Cryst. Growth 464, 28 (2017).
[18] L. Yang, M. T. Bulsara, K. E. Lee, and E. A. Fitzgerald, J. Cryst. Growth 324(1), 103 (2011).
[19] W. Metaferia, H. Kataria, Y.-T. Sun, and S. Lourdudoss, J. Phys. D 48(4), 045102 (2015).
[20] Y. Han, Y. Xue, and K. M. Lau, Appl. Phys. Lett. 114(19), 192105 (2019).
[21] S. Sharan, J. Narayan, and J. Fan, J. Electron. Mater. 20, 779 (1991).
[22] A. E. Romanov, W. Pompe, S. Mathis, G. E. Beltz, and J. S. Speck, J. Appl. Phys. 85(1), 182 (1999).
[23] B. Shi and J. Klamkin, J. Appl. Phys. 127(3), 033102 (2020).
[24] Y. Okuno and T. Kawano, J. Cryst. Growth 145(1–4), 338 (1994).
[25] D. Lubyshev, W. K. Liu, T. R. Stewart, A. B. Cornfeld, X. M. Fang, X. Xu, P. Specht, C. Kisielowski, M. Naidenkova, M. S. Goorsky, C. S. Whelan, W. E. Hoke, P. F. Marsh, J. Mirecki Millunchick, and S. P. Svensson, J. Vac. Sci. Technol. B 19(4), 1510 (2001).
[26] D. Kohen, X. S. Nguyen, R. I. Made, C. Heidelberger, K. H. Lee, K. E. K. Lee, and E. A. Fitzgerald, J. Cryst. Growth 478, 64 (2017).
[27] R. Alcotte, M. Martin, J. Moeyaert, R. Cipro, S. David, F. Bassani, F. Ducroquet, Y. Bogumilowicz, E. Sanchez, Z. Ye, X. Y. Bao, J. B. Pin, and T. Baron, APL Mater. 4(4), 046101 (2016).
[28] N. J. Quitoriano and E. A. Fitzgerald, J. Appl. Phys. 102(3), 033511 (2007).

20 August 2024 16:27:56

© Author(s) 2024